

Statistics of turbulent boundary layers computed by LES of a NACA0012 airfoil

Gabriel B. Nogueira*, Túlio R. Ricciardi† and William R. Wolf‡

University of Campinas, Campinas, SP, 13083-860, Brazil

In this work, we perform wall-resolved large eddy simulations to analyze the statistics of airfoil turbulent boundary layers. The impact of different tripping arrangements is assessed for a baseline Reynolds number $Re_c = 408,000$ based on the airfoil chord. The tripping configurations include two and three-dimensional square profiles and a random tripping composed of several spanwise wavenumbers with phase variations. A study of anisotropy is presented through analysis of the Lumley triangle, Reynolds stress anisotropy tensor, scatter plots of velocity components and probability density functions. The role of different tripping configurations is also discussed for budgets of turbulent kinetic energy. An initial assessment of different Reynolds number flows computed using the random tripping is also presented.

I. Introduction

STUDIES of flows past airfoil profiles find application in the design of aircraft wings, industrial rotors [1], and wind and gas turbines for energy production [2, 3]. More recently, airfoil flows have also been studied for the design of micro-air-vehicles (MAVs) [4] when the interest is in mimicking the flight and performance of birds and insects. Airfoil flows are also important for developing unmanned aerial vehicles (UAVs) with reduced drag and noise.

Most applications of the airfoil flows described above occur at sufficiently high Reynolds numbers for which the boundary layers and wakes are turbulent. In order to understand the characteristics of different airfoils for a range of applications, a study of turbulence properties for such flows is necessary. In this work, we employ wall-resolved large eddy simulations (LES) of turbulent flows past a NACA0012 airfoil at 5 degrees angle of incidence. Although there are several studies of free shear flows and channels [5] in the literature, applications of compressible wall-resolved LES to airfoils are more scarce. Differently from channel flows, airfoils have finite chords and, hence, represent a combination of wall-bounded turbulent flows with free shear flows. The wall effects found in channel flows are also present in airfoil flows but, for the latter, variations in the pressure gradient may induce changes in the flow statistics. Airfoil flows may also be heavily tripped to mimic wind tunnel experiments, a condition that is not typically found in channel flows. Such tripping mechanism may introduce different turbulent structures in the flow which play important roles in noise generation and drag [6].

In this work, we present a study of turbulence in flows over a NACA0012 airfoil. The aim here is to understand the flow statistics due to different tripping arrangements. Flow simulations are performed for a baseline case at Reynolds number $Re_c = 408,000$. The tripping arrangements analyzed consist of suction and blowing applied by two and three-dimensional square profiles besides a random tripping composed of several spanwise wavenumbers with phase variations. Flow statistics are ady presented for different Reynolds numbers. A study of anisotropy is presented through analysis of the Lumley triangle, Reynolds stress anisotropy tensor, scatter plots of velocity components and probability density functions. The role of different tripping configurations is also discussed for budgets of turbulent kinetic energy. An initial assessment of different Reynolds number flows computed using the random tripping is also presented.

II. Numerical Methodology

The present LES calculations solve the compressible Navier Stokes equations in conservative form using general curvilinear coordinates. The equations are written in conservation form as

$$\frac{\partial(\sqrt{g}\rho)}{\partial t} + \frac{\partial(\sqrt{g}\rho u^i)}{\partial \xi^i} = 0, \quad (1)$$

*MSc Student, Department of Energy, School of Mechanical Engineering

†PhD Candidate, Department of Energy, School of Mechanical Engineering

‡Assistant Professor, Department of Energy, School of Mechanical Engineering, AIAA Member

$$\frac{\partial(\sqrt{g}\rho u^i)}{\partial t} + \frac{\partial[\sqrt{g}(\rho u^i u^j + g^{ij} p - \tau^{ij})]}{\partial \xi^j} = -\Gamma_{jk}^i \sqrt{g}(\rho u^k u^j + g^{kj} p - \tau^{kj}), \quad (2)$$

$$\frac{\partial(\sqrt{g}E)}{\partial t} + \frac{\partial \sqrt{g}[(E + p) u^j - \tau^{ij} g_{ik} u^k + q^j]}{\partial \xi^j} = 0, \quad (3)$$

where u^i , ρ , and p are the contravariant velocity components, density, and pressure, respectively. The total energy E , the viscous stress tensor τ^{ij} , and the heat flux q^j for a fluid obeying Fourier's law are given by

$$E = \frac{p}{\gamma - 1} + \frac{1}{2} \rho g_{ik} u^i u^k, \quad (4)$$

$$\tau^{ij} = \frac{\mu}{Re} \left(g^{jk} \frac{\partial u^i}{\partial \xi^k} + g^{ik} \frac{\partial u^j}{\partial \xi^k} - \frac{2}{3} g^{ij} \frac{\partial u^k}{\partial \xi^k} \right), \quad (5)$$

and

$$q^j = -\frac{\mu}{Re Pr} g^{ij} \frac{\partial T}{\partial \xi^i}. \quad (6)$$

Assuming the medium to be a calorically perfect gas, the set of equations is closed by the equation of state

$$p = \frac{\gamma - 1}{\gamma} \rho T. \quad (7)$$

In the previous equations, g_{ij} and g^{ij} are the covariant and contravariant metric tensors, respectively, \sqrt{g} is the determinant of the Jacobian transformation matrix and Γ_{jk}^i represents the Christoffel symbols that appear due to grid curvature. The equations are solved in nondimensional form where length, velocity components, density, pressure, and temperature are nondimensionalized by a reference airfoil chord C , freestream speed of sound c_∞ , freestream density ρ_∞ , $\rho_\infty c_\infty^2$, and $(\gamma - 1)T_\infty$, respectively. Here, T is the temperature; γ is the ratio of specific heats; Re is the Reynolds number, defined as $Re = Re_a M_\infty$, where $Re_a = \rho_\infty c_\infty C / \mu_\infty$ and $M_\infty = U_\infty / c_\infty$; Pr is the Prandtl number, defined as $Pr = \mu_\infty c_p / \kappa_\infty$; c_p is the heat capacity at constant pressure; μ is the viscosity coefficient and κ is the thermal conductivity coefficient.

The spatial discretization of the equations is performed using a compact scheme of sixth order accuracy [7] implemented on a staggered mesh. Compact finite difference schemes are non-dissipative and, consequently, there is a need for filtering the solution since numerical instabilities may grow due to non-uniform meshes and numerical discretization errors. The current filter is applied only at high wavenumbers in order to preserve the most energetic scales [8]. In the present simulations, we make use of overset grids with a fourth-order accurate Hermite interpolation between grid blocks [9] in order to better resolve the boundary layers and wakes along the airfoil.

The temporal integration of the equations is carried out by a second-order scheme of Beam and Warming [10] in the near-wall region in order to overcome the time step restriction typical of boundary layer grids. Away from solid walls, we advance the solutions in time using a compact storage third-order Runge-Kutta scheme. In the wall boundaries, the non-slip condition is employed for an adiabatic wall except for the tripping regions. In the spanwise direction we employ a periodic boundary condition and, in the farfield, boundary conditions are based on characteristic variables besides the application of a buffer layer that prevents acoustic wave reflections.

III. Flow and Mesh Configurations

Tripping effects are first studied for a baseline flow configuration run at Reynolds number $Re = 408,000$ and freestream Mach number $M_\infty = 0.115$. The airfoil is set at 5 degrees angle of attack and results are compared to previous studies by Wolf [11]. All mesh configurations consist of body-fitted O-grid blocks designed to resolve the turbulent boundary layer on the suction side of the airfoil. The O-grid blocks have a higher concentration of points (approximately 75%) in the suction side and use a mesh stretching generated by a hyperbolic tangent function in the wall-normal direction. In the background, a Cartesian grid with uniform resolution around the O-grid is employed using an overset mesh procedure. Figure 1 shows a comparison of the meshes used in the current investigation. Detail views of the O-grids can also be seen in the figures, which show every 6 points to allow a better visualization of the meshes. In Fig. 1 (d), the vertical divisions in the O-mesh are due to the output format which facilitates the mesh visualization and post-processing in zones. Table 1 presents details of the mesh configurations employed in the simulations.

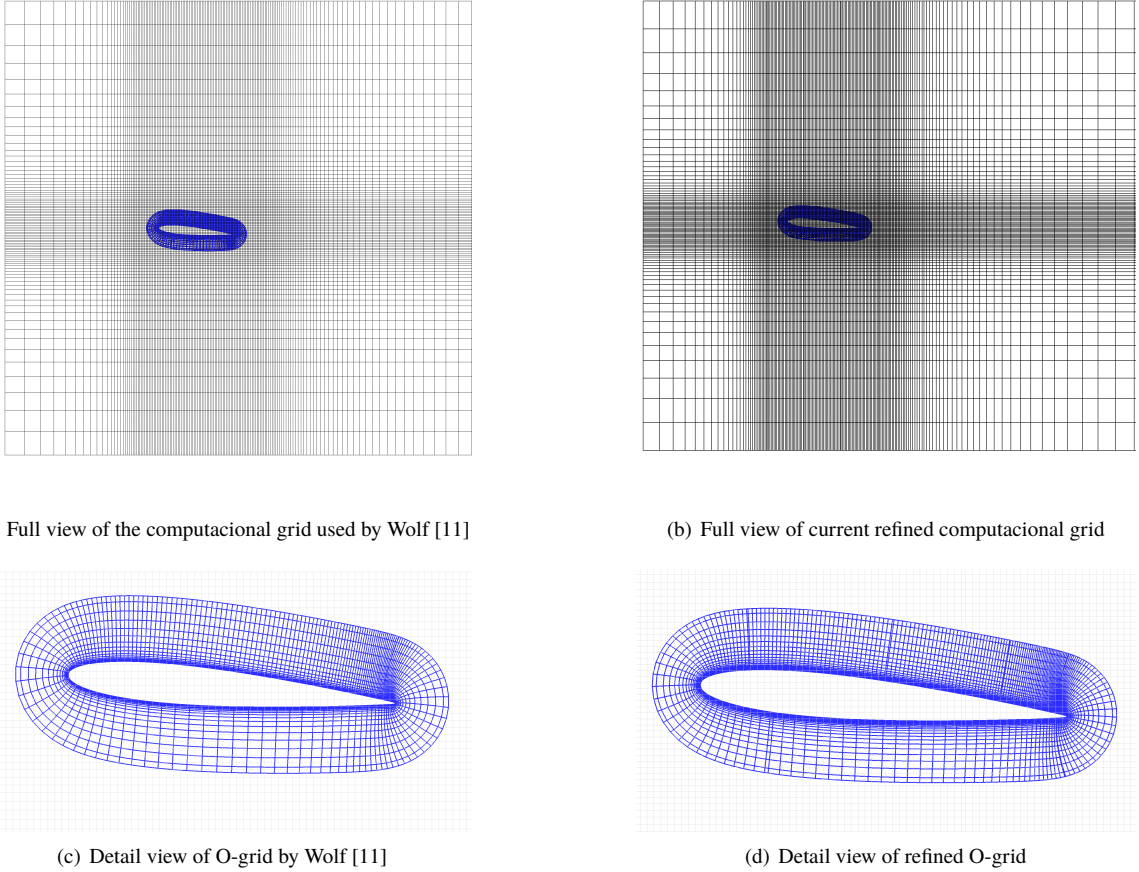


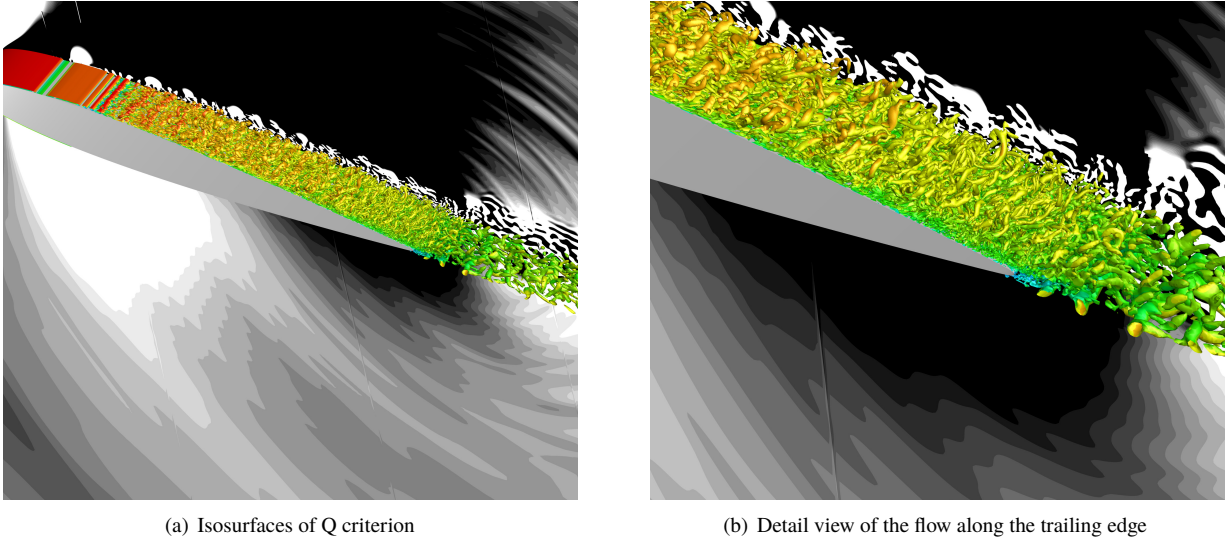
Fig. 1 Comparison of different grids for NACA0012 airfoil (every 6th grid point shown).

Results in terms of iso-surfaces of Q-criterion are presented in Fig. 2. These results are obtained for the mesh shown in Fig. 1(b) and it is possible to observe the development of the turbulent boundary layer along the suction side of the airfoil. For this case, the tripping is two-dimensional and some 2D structures form downstream of the tripping region. Later, these structures are disturbed transitioning to a fully turbulent regime as can be seen in the detailed view of the trailing edge region.

A. Tripping Configuration

Different tripping configurations are tested in order to disturb the boundary layer. Two-dimensional and three-dimensional steady tripping arrangements are employed along the airfoil suction side, near the leading edge. Suction is applied at $0.15 < x/c < 0.175$ and blowing at $0.175 < x/c < 0.20$ to mimic the experiments by [12]. Both suction and blowing have magnitudes $U_{blowing} = -U_{suction} = 0.03 U_\infty$, where U_∞ represents the freestream velocity. Due to tripping and an adverse pressure gradient, the boundary layer becomes turbulent on the suction side of the airfoil. On the pressure side, the boundary layer remains laminar since no tripping is applied in this region and the flow has a favorable pressure gradient.

Wolf [11] employed a three-dimensional spanwise tripping that consisted of a squared-wave at $10\% < z/s < 90\%$. Here, we also test a two-dimensional version of the same square wave as discussed in Ricciardi et al. [13]. In order to identify possible "artificial" non-physical structures caused by the previous tripping configurations (3D and 2D), a random tripping is also employed with variations in space and time. The function that determines the distribution of random tripping along the span is composed by a harmonic function, where wavenumbers are excited up to the spanwise



(a) Isosurfaces of Q criterion

(b) Detail view of the flow along the trailing edge

Fig. 2 Iso-surfaces of Q criterion for the flow configuration with 2D tripping.

Nyquist frequency

$$S(z) = \sum_{k=1}^{Nz/2} 0.03 U_\infty \text{rand}(A) \sin(kz + \phi) , \quad -1 \leq A \leq 1 . \quad (8)$$

A random amplitude A modulates the velocity of the tripping region and a Gaussian distribution is used to smooth out the disturbance along the flow direction along the tripping region. Solutions obtained by the different tripping setups are shown in Fig. 3 and Table 1 presents details of the tripping configurations investigated.

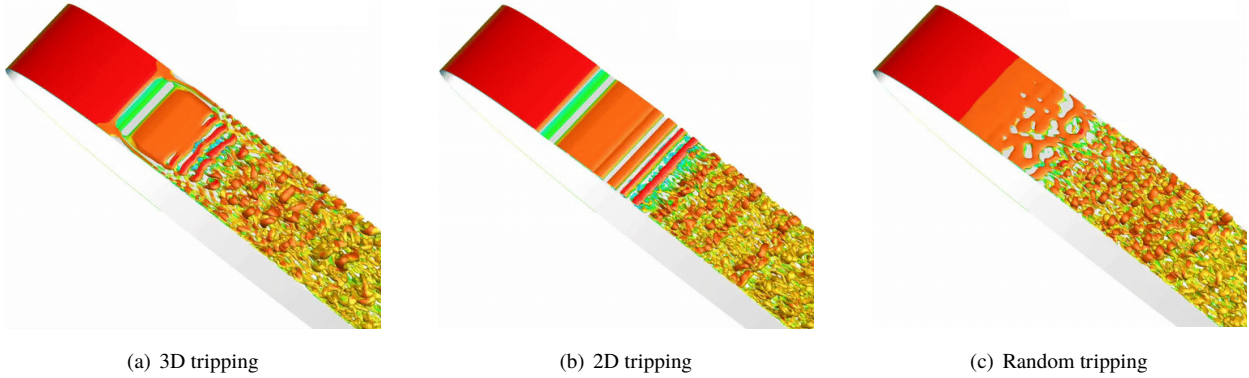


Fig. 3 Comparison of different tripping configurations.

IV. Results and Discussion

Figure 4 (a) shows the surface distribution of friction coefficient defined as $C_f = \frac{\tau_w}{(1/2\rho U_e^2)}$. Here, τ_w is the wall shear stress and U_e is the velocity at the edge of the boundary layer. As can be seen, all simulations present good agreement in terms of C_f near the trailing edge. However, results show considerable differences near the tripping location. For the 2D tripping, there is a region of negative friction coefficient which indicates the appearance of a small recirculation bubble just downstream the blowing region. The 3D square wave tripping keeps the flow absent from this bubble probably because of longitudinal vortical structures that add momentum to the flow near the periodical boundary conditions.

Table 1 Different meshes and tripping configurations. The values n_x, n_y, n_z represent the number of points in the x, y, z directions, respectively. The terms $\Delta x_w^+, \Delta y_w^+$ and Δz_w^+ correspond to the mesh resolution on the first element near the airfoil surface, in viscous units. The subscripts “max” and “TE” represent maximum values computed along the airfoil surface and those near the airfoil trailing edge, along the suction side.

Simulations	O -grid (n_x, n_y, n_z)	$\Delta x_{w_{max}}^+$	$\Delta y_{w_{max}}^+$	$\Delta z_{w_{max}}^+$	$\Delta x_{w_{TE}}^+$	$\Delta y_{w_{TE}}^+$	$\Delta z_{w_{TE}}^+$	Tripping
1	960 x 125 x 128	63.5	0.63	21	14.5	0.39	13	3D
2	1200 x 190 x 144	50.5	0.58	18	11	0.37	11.5	2D
3	960 x 125 x 128	63.5	0.63	21	14.5	0.39	13	Random

The random tripping provides the least intrusive results since it transitions the flow with minimal variation in friction coefficient. Figure 4 (b) shows the distribution of pressure coefficient C_p along the airfoil surface. Results are compared to the simulation by Wolf [11], an Xfoil solution[14] and potential flow theory. As can be noticed, there is a good agreement among all results. Xfoil captures a stronger suction peak at the leading edge but, overall, solutions are similar. Similarly to the friction coefficient, the pressure coefficient is also smoothed out for the random tripping solution.

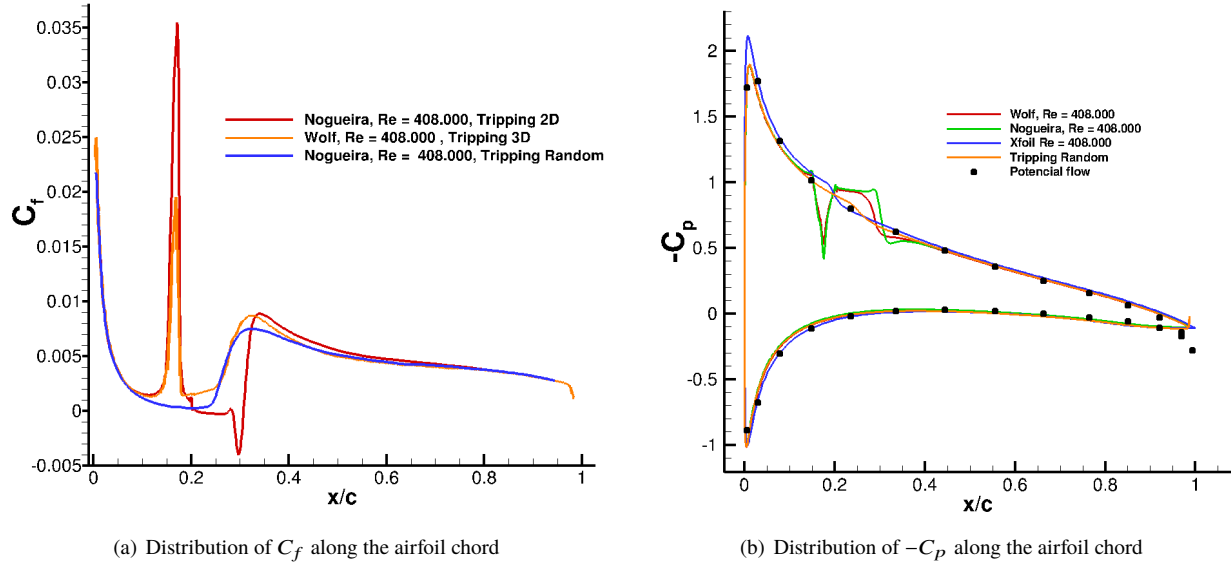


Fig. 4 Distribution of C_f along the airfoil chord (a) and $-C_p$ along the airfoil chord (b).

Figure 5 shows the mean velocity profiles at $x/c = 0.9$ normalized by friction velocity as function of wall units y^+ . As in Wolf [11], the log-law regions present shifts in the mean velocity profiles when compared to the standard log law. In the same figure, one can see the mean velocity profiles of Ricciardi et al. [13] obtained with the two-dimensional tripping in the suction side and for the random tripping. Results demonstrate that the tripping configurations do not have a considerable impact on the mean velocity profiles. A mesh refinement is employed and causes a small change in the slope of the log region when compared to the typical von Kármán slope obtained for a flat plate.

Although the mean velocity profiles do not agree with the classical log law for flat plates, we show that the current results match experimental data obtained for NACA0012 airfoils at similar flow conditions [15]. Therefore, possible variations of pressure gradients on the airfoil, as well as curvature and Reynolds number effects, may shift the profiles for the current airfoil flows compared to the standard log law.

In Fig. 6, the distributions of Reynolds stresses normalized by friction velocity are presented for different tripping configurations at the position $x/c = 0.90$. As one can see, results obtained for the 2D, 3D and random trippings are similar. However, one should note that for the Reynolds stress component $\langle u_1 u_1 \rangle$, the maximum value for the 2D tripping has a smaller magnitude compared to the other cases.

In order to investigate the effects of turbulence anisotropy, the Reynolds stresses are characterized by trajectories of

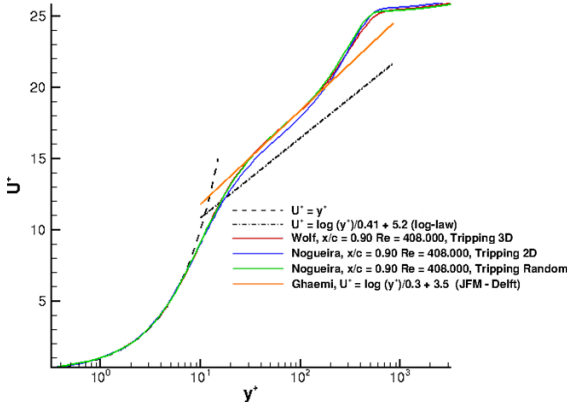


Fig. 5 Mean velocity profiles normalized by friction velocity.

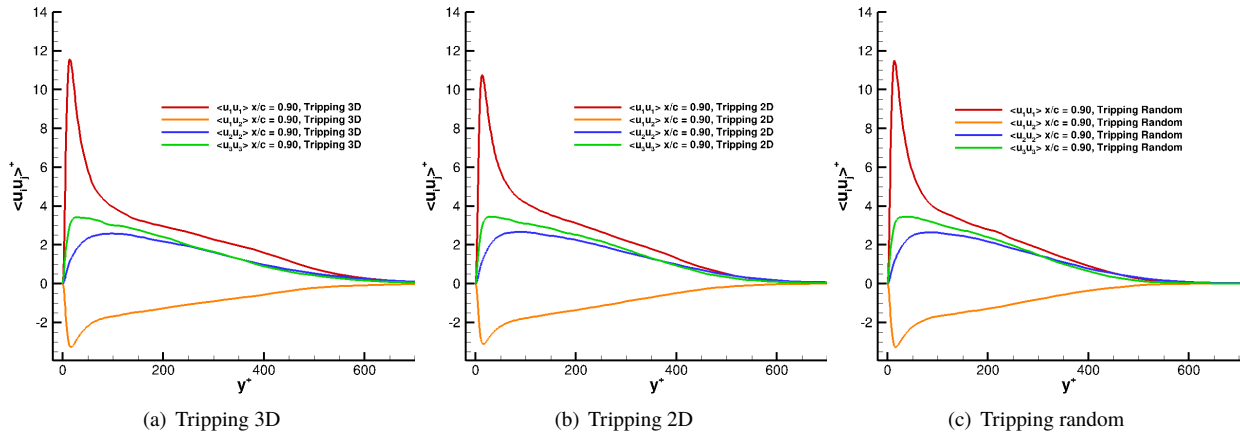


Fig. 6 Reynolds stresses normalized by friction velocity.

the invariant anisotropy tensor in the Lumley triangle [16]. All possible states of turbulence must be found within the Lumley triangle. Although the Lumley triangle assumes incompressibility, it is employed here due to the low freestream Mach number. The normalized Reynolds tensor b_{ij} is computed as

$$b_{ij} = \frac{\langle u'_i u'_j \rangle}{\langle u'_k u'_k \rangle} - \frac{\delta_{ij}}{3}. \quad (9)$$

Due to a normalization of the tensor b_{ij} when turbulence becomes isotropic all fluctuations u'_i have the same magnitude and the anisotropy tensor goes to zero. Non-zero values represent the degree of anisotropy in each principal direction. The invariants of the second-order tensor are given by I, II, III as:

$$I = b_{ii}, \quad II = -\frac{b_{ij} b_{ji}}{2}, \quad III = \frac{b_{ij} b_{jk} b_{ki}}{3}. \quad (10)$$

In order to verify the behavior of the return isotropy and its respective trajectory, Choi and Lumley [16] introduced new variables ξ and η so the turbulence triangle can also be transformed from the II-III coordinates to ξ - η coordinates. In this way, the isotropic behavior is observed in the origin of the ξ - η coordinate system. The upper limit of the triangle represents a state of 2-D turbulence, and the left and right sides of the triangle represent axisymmetric turbulence; one dimensional turbulence is found in the top corner of the triangle, on the right. The trajectories in the Lumley triangle at different positions along the airfoil chord are shown in Fig. 7.

The triangle is computed for different chord positions up to the limit of the boundary layer thickness. As can be seen, near the wall, the turbulence is two-dimensional since the wall-normal velocity fluctuations are negligible compared to

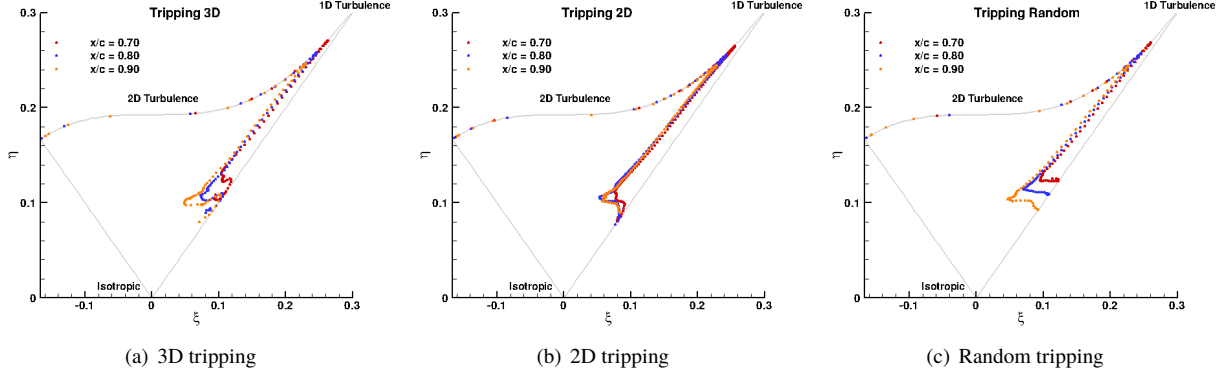


Fig. 7 Trajectories along the Lumley triangle for different positions and tripping configurations.

the other components. As y^+ increases, it approaches one-dimensional turbulence due to an increase of the velocity fluctuation u' in the buffer layer, where streaks are abundant and production reaches a peak. For $y^+ > 10$, turbulence becomes more three-dimensional towards the isotropic state. Also, one should notice that turbulence becomes more one-dimensional for positions further upstream along the airfoil chord.

Independently of the orientation of the coordinate system, for the Lumley triangle, the anisotropy is the same since it is obtained from the invariants of the normalized anisotropy tensor. Here, the normalized anisotropy tensor b_{ij} is obtained for a velocity field in the wall-normal and tangential directions. Through the profiles shown for position $x/c = 0.90$ in Fig. 8 it is possible to identify how the processes evolve along y^+ . Note that near the wall the tangential velocity fluctuations are predominant due to the streaks. The fluctuation of normal velocity is practically invariant up to $y^+ \approx 10$, which is the region of highest turbulence production and where the tangential components of the velocity fluctuations reach maximum values.

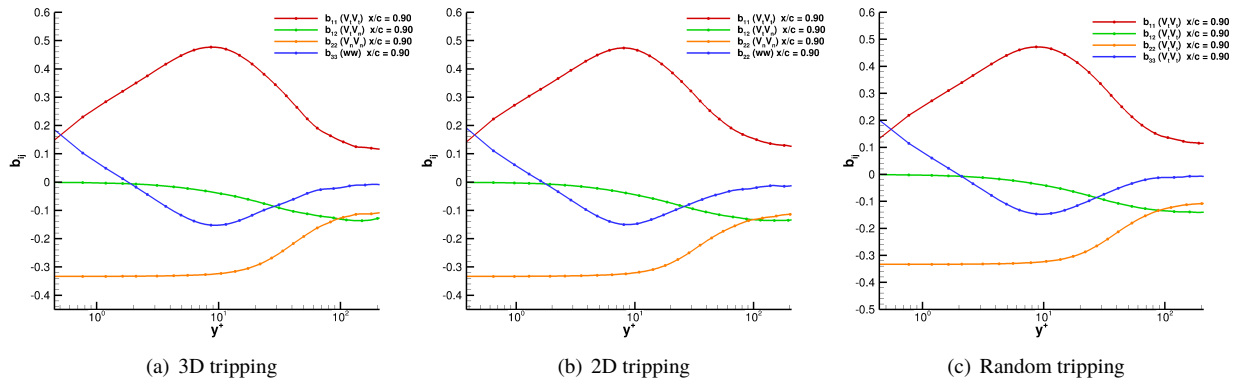


Fig. 8 Profiles of anisotropy tensor components for different tripping configurations.

Turbulent kinetic energy (TKE) budgets are computed to assess the individual effects of advection, production, turbulent transport, viscous diffusion, pressure diffusion, and pseudo-dissipation in the TKE budget. The temporal variation of TKE can be written as

$$\frac{\partial k}{\partial t} = A + P + T + D + D_p - \epsilon \quad (11)$$

where, for a statistically stationary flow, the time derivative must be zero. The terms in the right-hand side of this equation are defined as:

$$\text{Advection: } A = - \langle U_j \rangle \frac{\partial k}{\partial x_j}, \quad (12)$$

$$\text{Production: } P = - \left\langle u'_i u'_j \right\rangle \frac{\langle \partial U_i \rangle}{\partial x_j}, \quad (13)$$

$$\text{Turbulent transport: } T = -\frac{1}{2} \frac{\partial \langle u'_i u'_j u'_j \rangle}{\partial x_j}, \quad (14)$$

$$\text{Viscous diffusion: } D = \nu \frac{\partial^2 k}{\partial x_j^2}, \quad (15)$$

$$\text{Pressure diffusion: } D_p = -\frac{1}{\rho} \frac{\partial \langle u_i p' \rangle}{\partial x_i}, \quad (16)$$

$$\text{Pseudo-dissipation: } \epsilon = -\nu \left(\frac{\partial u_i}{\partial x_j} \frac{\partial u_i}{\partial x_j} \right). \quad (17)$$

Results are shown for different tripping configurations in Fig. 9. The TKE budgets are made non-dimensional by the

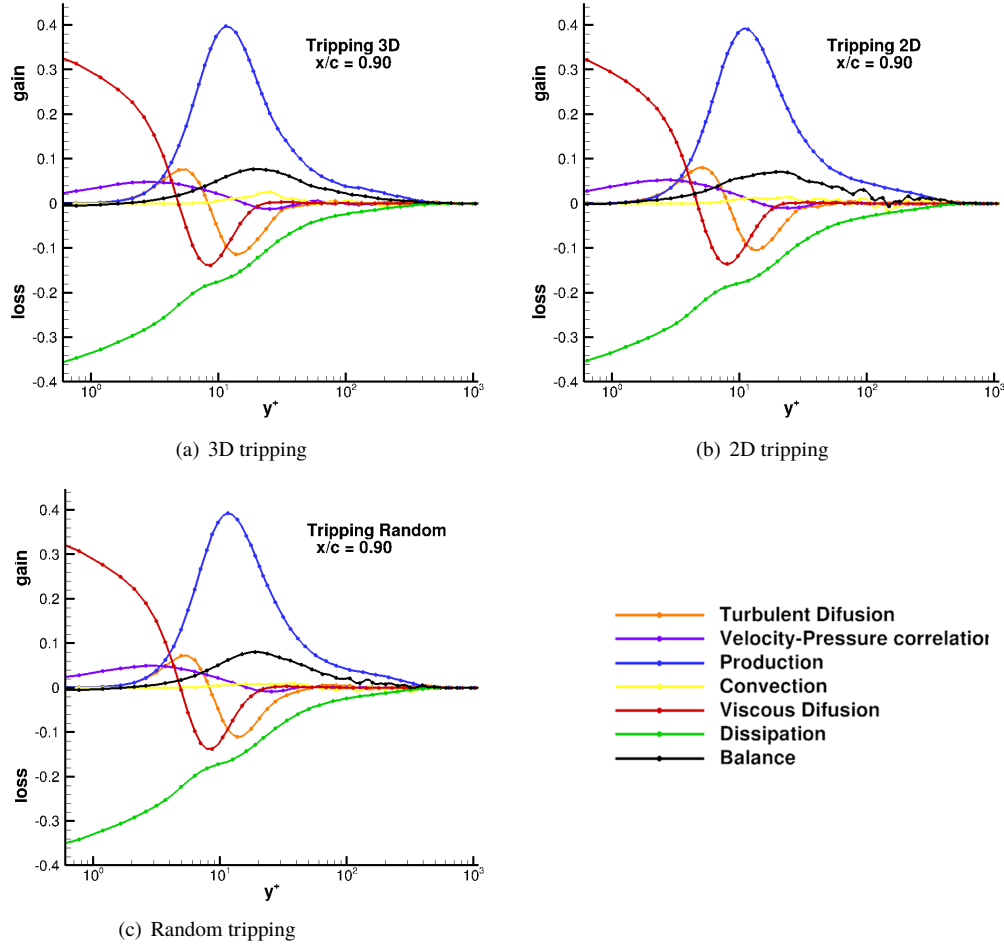


Fig. 9 TKE budgets for different tripping configurations at $x/c = 0.90$.

factor of $\frac{u'^4}{\nu}$ [5]. One should first notice that, very close to the wall, the kinetic energy balance is zero. Note also that for $y^+ \approx 10$ there is the highest level of turbulence production. At $y^+ \approx 20$ there is the largest error in the TKE balance and this difference is attributed to the filtered scales in the LES which are not present in the pseudo-dissipation term. The behavior of TKE for the 3D, 2D, and random tripping are very similar, with a significant increase mainly in the terms of the turbulent transport and viscous diffusion in the 3D and random tripping.

In wall-bounded turbulence, streaks and hairpins are frequently analyzed and these coherent structures are directly affected by sweeps and ejections that occur in the boundary layer induced by outboard and inboard flows. Such

observations are evidenced in the following scatter plots of velocity fluctuations. In the scatter plots, data is normalized

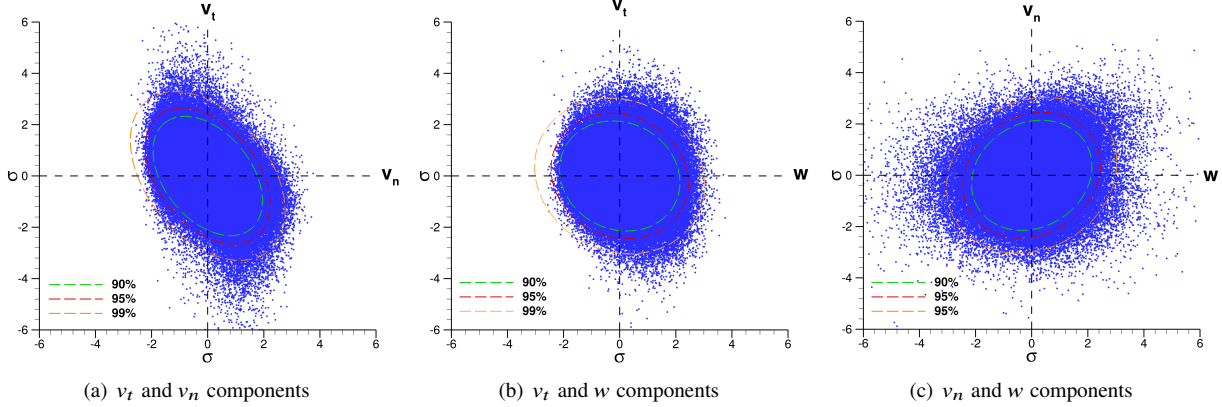


Fig. 10 Distribution of velocities normalized by standard deviation at $x/c = 0.90$ and $y^+ = 10$.

by the respective standard deviation and the curves are presented for the random tripping configurations since all tripping configurations exhibited the same behavior. We show results for $x/c = 0.90$ and $y^+ = 10$ which correspond to the peak of maximum turbulence production in the kinetic energy budget. Covariance error ellipses are also shown for 90%, 95% and 99% values. The distributions of velocity fluctuations uw and vw are more circular and uniform due to the spanwise homogeneity, unlike uv , which has a preferred direction typical of the principal Reynolds shear stresses. One can see from the plots that sweeps and ejections occur for the Q_4 and Q_2 quadrants, respectively, with more extreme values of ejections at $y^+ = 10$.

The same physical mechanism of ejections and sweeps is also evident when computing probability density functions (PDFs). Here, the PDFs are obtained for the random tripping at $x/c = 0.90$ for $y^+ = 5, 10, 15, 20, 50$ and 100 . All PDFs are normalized by their respective standard deviations. A kernel distribution is used to provide a nonparametric representation of the PDF, which is written as a function of the kernel as

$$f_h(V) = \frac{1}{nh} \sum_{i=1}^n K\left(\frac{v - v_i}{h}\right), \quad (18)$$

where v_1, v_2, \dots, v_n are random samples from an unknown distribution, n is the sample size, $K(\cdot)$ is the kernel smoothing function, and h is the bandwidth. The distributions for velocity fluctuations v_t , v_n and w are shown respectively in Fig. 11.

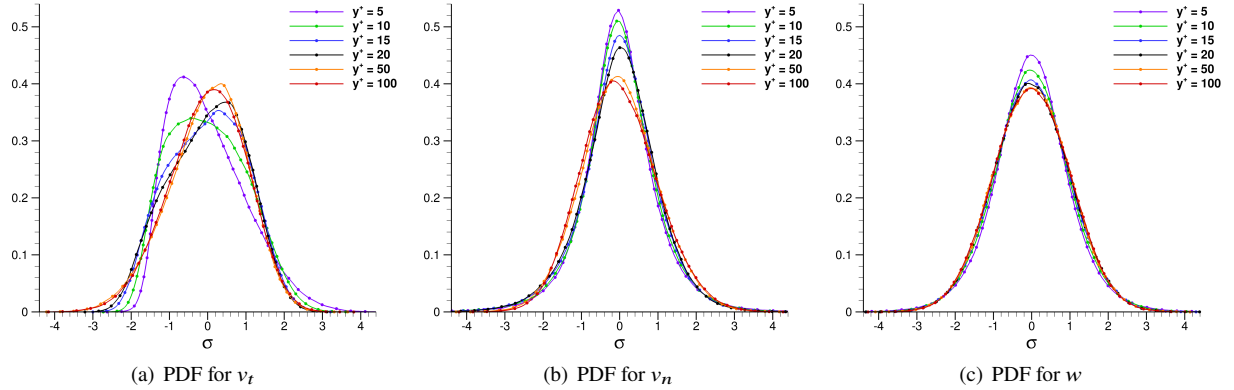


Fig. 11 PDF for v_t , v_n and w components at $x/c = 0.90$.

The results for the PDFs are compared with Wacławczyk et al. [17] and Dinavahi [18], who present results obtained for a turbulent channel flow, and they exhibit good agreement. For the tangential velocity v_t we note the change in

positive skewness (associated with ejections) to a negative skewness (associated with sweeps) along the boundary layer. This mechanism also occurs for the normal velocity v_n , however, it is more subtle for skewness. On the other hand, kurtosis will change with increasing y^+ , approaching the typical value of 3 for a Gaussian distribution. As expected, the PDF of w velocity component is a Gaussian distribution as can be also inferred from its skewness and kurtosis.

Once the impact of different tripping configurations is studied, additional simulations are carried out in order to verify the impact of the Reynolds number on the flow statistics. The simulation setups are shown in Table 2 and consider three Reynolds numbers, $Re = 2 \times 10^5$, 4×10^5 and 8×10^5 . For these simulations, only the random tripping is tested due to the smoother behavior of the C_f and C_p curves previously shown. Similar mesh configurations are employed in the simulations, with improvements in resolution to resolve the flow features. The mesh parameters can also be seen in Table 2. The resolution properties follow the best practices for LES as discussed by Wagner et al. [19] and are shown in Fig. 12. In particular, it is noted that for the Re800k simulation the positioning of the tripping is placed slightly upstream since natural transition occurs earlier for this Reynolds number.

Table 2 Different setups investigated.

Simulations	O-grid (n_x, n_y, n_z)	Background-grid (n_x, n_y, n_z)	Tripping position	Span
Re 200k	960 x 125 x 252	896 x 511 x 126	$0.15 \leq x/c \leq 0.20$	$0.19\bar{c}$
Re 400k	960 x 125 x 128	896 x 511 x 64	$0.15 \leq x/c \leq 0.20$	$0.10\bar{c}$
Re 800k	1600 x 220 x 210	960 x 529 x 105	$0.09 \leq x/c \leq 0.14$	$0.08\bar{c}$

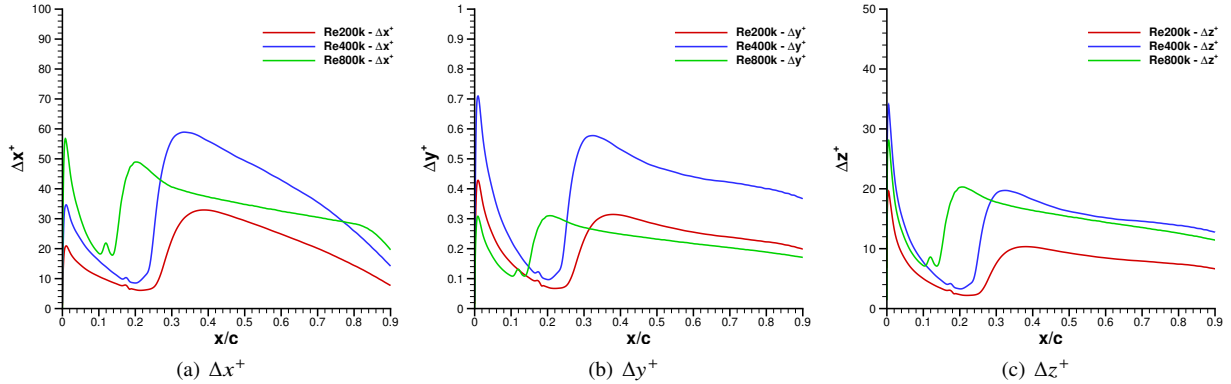


Fig. 12 Mesh resolution in the wall region for different Reynolds numbers.

Results for different Reynolds numbers are shown in Fig. 13 in terms of iso-surfaces of Q-criterion. One can observe the development of turbulent boundary layers with finer scales for the higher Reynolds numbers. The span widths are also adjusted compared to the baseline configuration in order resolve at least 3 boundary layer thicknesses. Values of boundary layer thickness are estimated a priori using XFOIL.

The pressure and friction coefficients C_p and C_f are shown in Fig. 14. It is possible to notice that the pressure distribution along the airfoil is practically the same for the different Reynolds numbers. On the other hand, the Reynolds number has a severe impact on the friction coefficient distributions. First, one can see that the flow transitions earlier for $Re = 8 \times 10^5$. This is due to the higher Reynolds number and also the tripping position, which is placed further upstream compared to the other cases to avoid natural transition.

One of the essential parameters in wall-bounded turbulent flows is the pressure gradient that directly affects the dynamics of the boundary layer. Several recent works try to characterize the pressure gradient in airfoils [20–22]. However, this is still a subject of research since the determination of the velocity at the edge of the boundary layer is non-trivial when it is subjected to strong pressure gradients and curvature. Here, the parameter that defines the effect of the adverse pressure gradient is the Clauser parameter $\beta = \delta^*/\tau_w dP_e/dx_t$, where δ^* is the displacement thickness and P_e is the pressure at the edge of the boundary layer [23]. The variations in β along the airfoil surface are shown in Fig. 15 together with the friction Reynolds number Re_τ and the momentum thickness Reynolds number Re_θ . While

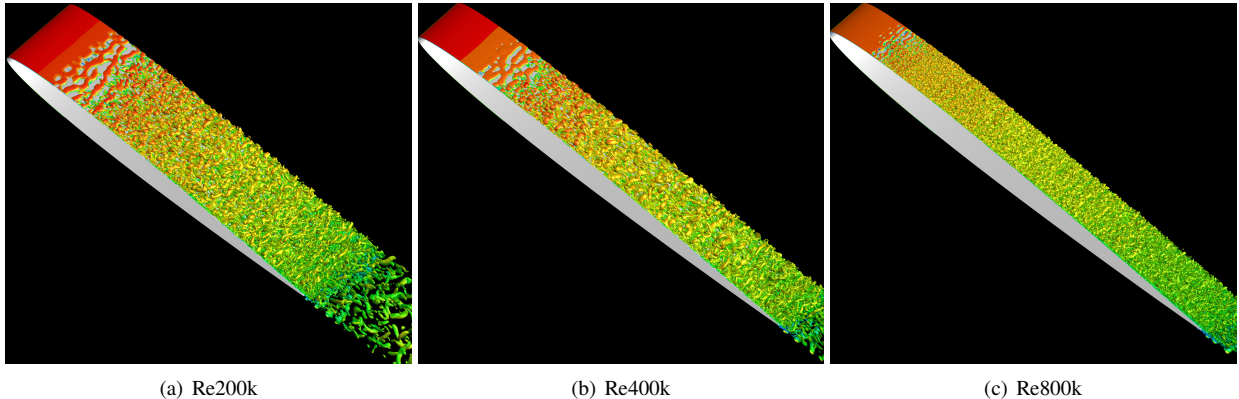


Fig. 13 Isosurfaces of Q criterion for different Reynolds numbers .

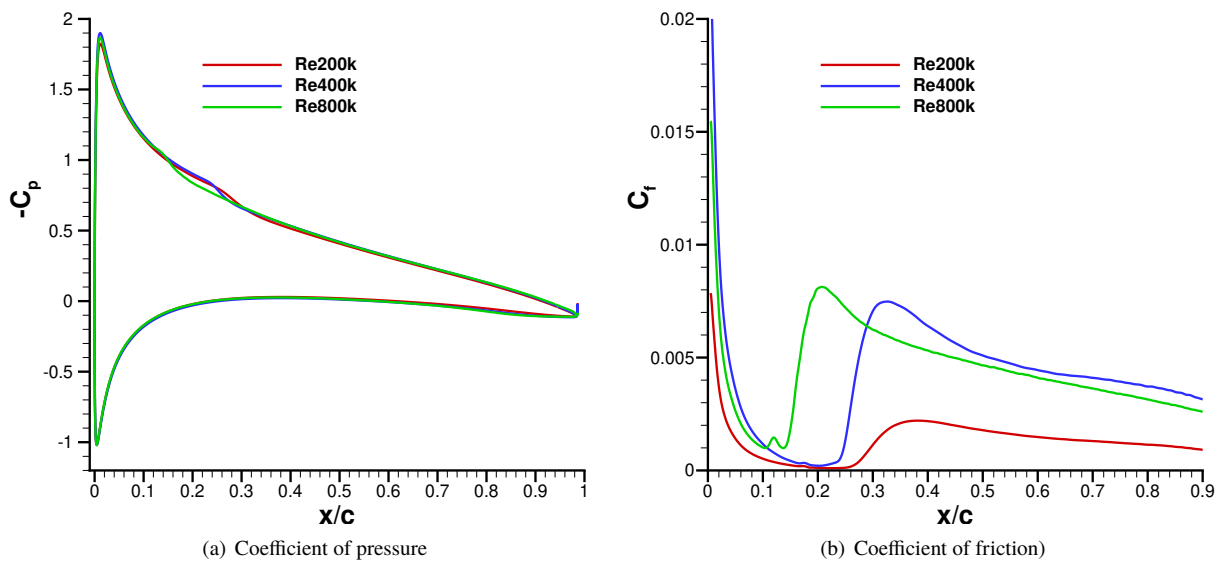


Fig. 14 Coefficient of pressure and friction for different Reynolds numbers.

Re_τ is computed using the friction velocity and boundary layer thickness, Re_θ employs the edge velocity U_e , which is computed at the edge of the boundary layer, set to 99% of the maximum tangential flow velocity, and the momentum thickness θ . This last parameter is calculated by

$$\theta = \int_0^\delta \frac{U_t}{U_e} \left(1 - \frac{U_t}{U_e} \right) dy . \quad (19)$$

where U_t is the tangential velocity. Results presented in Fig. 15 are in good agreement with results from Tanarro et al. [20].

V. Conclusions

In the current work we employ wall-resolved large eddy simulations to study turbulent flows over a NACA 0012 airfoil. Statistics of the turbulent flows are presented in terms of TKE budgets and anisotropy through analysis of the Reynolds stress anisotropy tensor, Lumley triangle and PDFs. We also show comparisons in terms of pressure and friction coefficients, as well as mean velocity and Reynolds stress profiles. Different boundary layer tripping

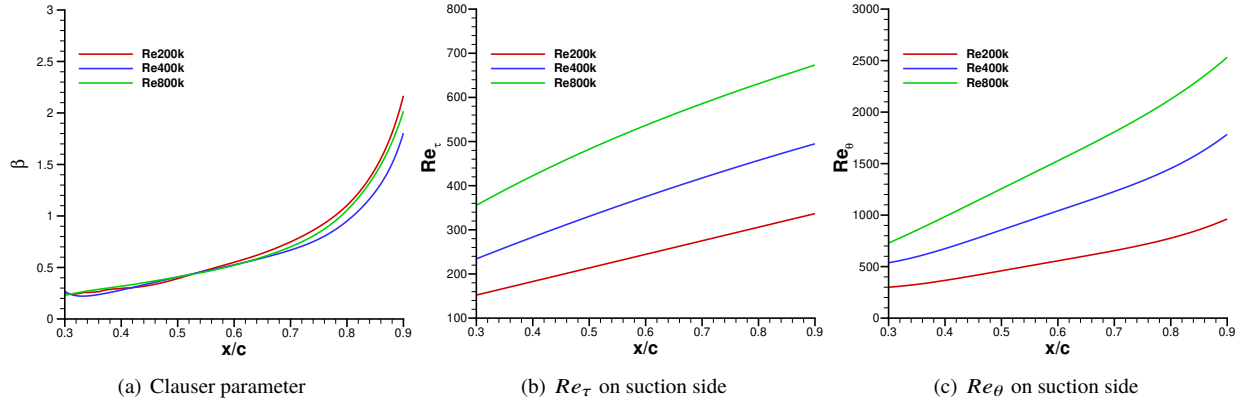


Fig. 15 Non-dimensional parameters for different Reynolds numbers.

configurations are tested and results show agreement for all arrangements, with some subtle changes in some of the statistics. We observe in the Lumley triangle that the route to isotropy is slightly different from that typically found in plane channel flows. Statistics obtained by the 3D, 2D and random trippings are similar for the current analyses despite that, for the 2D tripping configuration, a small separation bubble is observed just downstream of the tripping location. On the other hand, for the 3D tripping, the flow is fully attached, probably because of longitudinal vortices generated due to tripping and that add streamwise momentum to the flow. The random tripping is more recommended to disturb the boundary layer as shown on C_f and C_p distributions since it is less intrusive. However, it is not recommended for acoustic analysis due to its unsteady nature and inherent noise generation. The physical mechanism of ejections and sweeps is evidenced in scatter plots and PDFs. A preliminary analysis is also presented for different Reynolds number flows and further investigations will be conducted in future work.

Acknowledgments

The authors acknowledge the financial support received from Fundação de Amparo à Pesquisa do Estado de São Paulo, FAPESP, under Grants No. 2013/08293-7, 2013/07375-0, and 2018/11835-0, and from Conselho Nacional de Desenvolvimento Científico e Tecnológico, CNPq, under Grants No. 304335/2018-5 and 407842/2018-7. We also thank LNCC (cluster SDumont) for providing the computational resources used in this work through project SimTurb. The authors also acknowledge the CAPES and FAPESP scholarships provided to the first and second authors of this work, respectively.

References

- [1] Gourdain, N., Singh, D., Jardin, T., and S. Prothin, "Analysis of the Turbulent Wake Generated by a Micro Air Vehicle Hovering near the Ground with a Lattice Boltzmann Method," *Journal of the american helicopter society*, Vol. 62, 2017, pp. 1–12.
- [2] Li, Y., Castro, A., Sinokrot, T., and Carrica, W. P. P., "Coupled multi-body dynamics and CFD for wind turbine simulation including explicit wind turbulence," *Elsevier*, Vol. 76, 2015, pp. 338–361.
- [3] Oerlemans, S., "Detection of aeroacoustic sound sources on aircraft and wind turbines," Ph.D. thesis, University of Twente, 2009.
- [4] Truong, T. V., Byun, D., Kim, M. J., Yoon, K., and C. Park, H., "Aerodynamic forces and flow structures of the leading edge vortex on a flapping wing considering ground effect," *IOP Science Journals*, Vol. 8, 2013.
- [5] Pope, S. B., *Turbulent Flows*, 1st ed., Cambridge University Press, New York, 2000.
- [6] Wolf, W. R., Azevedo, J. L. F., and Lele, S., "Convective Effects and the Role of Quadrupole Sources for Aerofoil Aeroacoustics," *Journal of Fluid Mechanics*, Vol. 708, 2012, pp. 502–538.
- [7] Nagarajan, Lele, S., S.K., and Ferziger, J., "A robust high-order method for large eddy simulation," *Journal of Computational Physics*, Vol. 191, 2003, p. 392–419.

- [8] Lele, S., “Compact finite difference schemes with spectral-like resolution,” *Journal of Computational Physics*, Vol. 103, 1992, pp. 16–42.
- [9] Bhaskaran, R., and S.K., L., “Large eddy simulation of free-stream turbulence effects on heat transfer to a high pressure turbine cascade,” *Journal of Turbulence*, Vol. 11, No. 1, 2010, pp. 1–15.
- [10] Beam, R., and Warming, R., “An implicit factored scheme for the compressible Navier-Stokes equations,” *AIAA Journal*, Vol. 16, 1978, pp. 393–402.
- [11] Wolf, W. R., “Airfoil aeroacoustics: LES and acoustic analogy predictions,” Ph.D. thesis, Stanford University, 2011.
- [12] Brooks, T. F., Pope, D. S., and Marcolini, M. A., “Airfoil Self-Noise and Prediction,” *Tech. rep., NASA Reference Publication*, Vol. 1218, 1989.
- [13] Ricciardi, T. R., Ribeiro, J. H. M., and Wolf, W. R., “Analysis of Coherent Structures in Large-Eddy Simulations of a NACA0012 Airfoil,” *AIAA Scitech 2019 Forum*, 2019.
- [14] Drela, M., “XFOIL: An Analysis and Design System for Low Reynolds Number Airfoils,” *Conference Notre Dame, Indiana, USA*, Vol. 54, 1989.
- [15] Ghaemi, S., and Scarano, F., “Counter-hairpin vortices in the turbulent wake of a sharp trailing edge,” *Journal of Fluid Mechanics*, Vol. 689, 2011, p. 317–356.
- [16] Choi, K., and Lumley, J. L., “The return to isotropy of homogeneous turbulence,” *Journal of Fluid Mechanics*, Vol. 436, 2001, p. 59–84.
- [17] Wacławczyk, M., Pozorski, J., and Minier, J., “Probability density function computation of turbulent flows with a new near-wall model,” *Physics of Fluids*, Vol. 16, 2004.
- [18] Dinavahi, S. P. G., “Probability Density Functions in Turbulent Channel Flow,” *Tech. rep., NASA Reference Publication*, 1992.
- [19] Wagner, C., Hüttl, T., and Sagaut, P. (eds.), *Large-Eddy Simulation for Acoustics*, Cambridge University Press, New York, 2009, p. 107.
- [20] Tanarro, ., Vinuesa, R., and Schlatter, P., “Effect of adverse pressure gradients on turbulent wing boundary layers,” *Journal of Fluid Mechanics*, Vol. 883, 2020.
- [21] Vinuesa, R., Bobke, A., Örlü, R., and Schlatter, P., “On determining characteristic length scales in pressure-gradient turbulent boundary layers,” *Physics of Fluids*, 2016.
- [22] Bobke, A., Örlü, R., Schlatter, P., and Vinuesa, R., “History effects and near equilibrium in adverse-pressure-gradient turbulent boundary layers,” *Journal of Fluid Mechanics*, Vol. 820, 2017.
- [23] Clauser, F. H., “Turbulent Boundary Layers in Adverse Pressure Gradients,” *Journal of the Aerospace Sciences*, Vol. 21, 1954, p. 91–108.